De novo lipogenesis alters the phospholipidome of esophageal adenocarcinoma

Nima Abbassi-Ghadi[1,2†], Stefan S. Antonowicz[1†], James S. Mckenzie[3], Sacheen Kumar[1,4.5], Juzheng Huang[1], Emrys A. Jones[1], Nicole Strittmatter[1], Gemma Petts[6], Hiromi Kudo[6], Stephen Court[1], Jonathon M. Hoare[1], Kirill Veselkov[1], Robert Goldin[6], Zoltán Takáts[3*], George B Hanna[1*]

1 Department of Surgery and Cancer, Imperial College London, London, UK
2 Royal Surrey County Hospital, Guildford, Surrey, UK
3 Department of Metabolism, Digestion and Reproduction, Imperial College London, London, UK
4 Department of Upper GI Surgery, Royal Marsden Hospital NHS Foundation Trust, London, UK
5 Division of Radiotherapy & Imaging, Institute of Cancer Research, London, UK
6 Centre for Pathology, Imperial College London, London, UK
†These authors contributed equally to this work

Running Title: The phospholipidome of esophageal adenocarcinoma
Keywords: DESI-MSI, esophageal adenocarcinoma, glycerophospholipids, lipidomics, phosphatidylglycerols,

Conflicts of interest: The authors declare no conflicts of interest

[*]**Co-corresponding Authors:**

Professor G B Hanna
Head of Department
10th Floor, QEQM, St Mary's Hospital
Praed St London,
W2 1NY
Tel/Fax: (+) 44 2078862124/66309
g.hanna@imperial.ac.uk

Professor Z Takats
Head of Division
6th floor, SAFB,
South Kensington campus
Prince Consort Rd, London, SW7 2BB
Tel/Fax: (+) 44 2075942760
z.takats@imperial.ac.uk

Financial support The authors would like to acknowledge funding from the European Research Council (DESI-JeDI Imaging Starting Grant; MASSLIP Consolidator Grant), the National Institute of Health Research (Imperial Biomedical Research Centre) and the National Institute of Health Research – London In Vitro Diagnostics.

Word count abstract: 232/250
Word count main body: 4727/5000
Total number of Figures: 5
Total number of Supplementary Figures: 4
Total number of Supplementary Tables: 4

Abstract

The incidence of esophageal adenocarcinoma is rising, survival remains poor, and new tools to improve early diagnosis and precise treatment are needed. Cancer phospholipidomes quantified with mass spectrometry imaging can support objective diagnosis in minutes using a routine frozen tissue section. However, whether mass spectrometry imaging can objectively identify primary esophageal adenocarcinoma is currently unknown and represents a significant challenge, as this microenvironment is complex with phenotypically similar tissue-types. Here we used desorption electrospray ionisation mass spectrometry imaging (DESI-MSI) and bespoke chemometrics to assess the phospholipidomes of esophageal adenocarcinoma and relevant control tissues. Multivariable models derived from phospholipid profiles of 117 patients were highly discriminant for esophageal adenocarcinoma both in discovery (area-under-curve = 0.97) and validation cohorts (AUC = 1). Among many other changes, esophageal adenocarcinoma samples were markedly enriched for polyunsaturated phosphatidylglycerols with longer acyl chains, with stepwise enrichment in pre-malignant tissues. Expression of fatty acid and glycerophospholipid synthesis genes was significantly upregulated, and characteristics of fatty acid acyls matched glycerophospholipid acyls. Mechanistically, silencing the carbon switch ACLY in esophageal adenocarcinoma cells shortened GPL chains, linking de novo lipogenesis to the phospholipidome. Thus, DESI-MSI can objectively identify invasive esophageal adenocarcinoma from a number of pre-malignant tissues and unveils mechanisms of phospholipidomic reprogramming. These results call for accelerated diagnosis studies using DESI-MSI in the upper gastrointestinal endoscopy suite as well as functional studies to

determine how polyunsaturated phosphatidylglycerols contribute to esophageal carcinogenesis.

Word count: 232/250

Introduction

Esophageal cancer is the eighth most common malignancy worldwide causing approximately 500,000 deaths per annum(1). The predominant subtype in Western countries is esophageal adenocarcinoma (EA), which is linked to esophageal acid reflux. The normal lower esophageal squamous epithelium is replaced with an intestinal-type columnar mucosa ("Barrett's metaplasia"), which can acquire dysplastic changes leading to EA(2). It is often detected at an advanced stage, with approximately 30% of patients amenable to curative treatment(3). Despite improvements in multi-modality treatment, five-year survival after treatment with curative intent remains 30-35%, and all-stage 5-yr survival is 14%(3). Therefore, new tools to facilitate early diagnosis and effective treatment are needed.

Despite extensive investigation of how metabolism contributes to cancer(4–6), lipids - which constitute 70% of the human metabolome - are relatively understudied(7). Most lipids are sequestered in bilayer membranes as glycerophospholipids (GPLs). There are six GPL classes based on their head moiety, with further variation in acyl lengths and desaturations. These features convey diversity to the GPL profile(8), which is often altered in cancer states(9–12). Their chemical and physical stability makes them attractive for biomarker studies. Functionally, GPL diversity impacts membrane characteristics and cellular signalling. For example, the GPLs phosphatidylinositols (PIs) mediate phosphatidylinositol-3 kinase (PI3K) signalling, which is one of the most commonly deregulated pathways in EA(13), whereas phosphatidylglycerols (PGs) have potent and contrasting effects on squamous cells' proliferation(14). Thus, measuring GPLs may provide diagnostic biomarkers with actionable therapeutic potential; however, species composition must be determined precisely.

Tissue phospholipidomics using traditional liquid chromatography mass spectrometry was inherently limited, as even small homogenates cannot eliminate non-target cell

contamination in complex microenvironments like cancer(15),(16). Mass spectrometry imaging (MSI)(17) addresses this, by providing spatially-resolved lipid analysis using tissue sections. This allows accurate phospholipid profiles to be derived from histologically pure areas. Desorption electrospray ionisation-MSI offers advantages over MSI approaches, due to range of lipids detected, minimal sample preparation, performance in ambient conditions and non-destruction of analysed tissue sections allowing for comparative histological analysis(18). Typically hundreds of pixels from several sampling zones per specimen are collected, such that each phospholipid profile comprises tens of thousands of mass spectra across a patient cohort. The clinical potential of this technique has been described, for example to assess surgical resection margins for breast(11), brain(19) and prostate(20) cancers. In lung cancer, GPL profiling has highlighted new therapeutic approaches(21). Previously, we showed that phospholipidomics could differentiate metastatic EA from lymph node tissue(22). However, the phospholipid profile of primary EA is currently unknown, and represents a significant challenge to MSI as the complexity of this microenvironment is extra-ordinary and neighbouring non-malignant tissues can be phenotypically similar.

Here we used DESI-MSI to compare the normal squamous and EA GPL profile, using paired samples from surgical specimens. Next we assessed the evolution of the EA GPL profile, by comparing normal, inflamed, metaplastic, dysplastic, and neoplastic cell types, which also served as an external validation cohort. We then investigated the mechanistic basis for these GPL signatures, by describing the corresponding fatty acid pool and genetic framework. Finally, we linked *de novo* lipogenesis to EA GPL characteristics, by silencing a deregulated lipogenic gene and assessing the phospholipidomic changes *in vitro.*

Methods

Patients

Approval for the study was obtained via National Research Ethics Service (Ref: 04/Q0403/119) and Imperial College Healthcare Tissue Bank institutional review boards (Project R14121), adhering to Declaration of Helsinki principles. Written informed consent was taken from every participant prior to collecting samples. Two independent cohorts were used, and the REMARK guidelines were followed for the recruitment of patients in this observational study(23). For Cohort 1, biopsies were collected from EA surgical specimens of consecutive patients undergoing treatment of curative intent at a single tertiary referral centre (St Mary's Hospital, Imperial College NHS Trust, London) between April 2012 and August 2014. Samples were taken from macroscopically identified tumour and matched healthy esophageal epithelium (MHEE) 5cm away from the tumour. Squamous tissue was selected as the initial control given the intention to apply DESI-MSI for screening surgical resection margins for cancer. Also, the selection of control tissue and distance from the tumour followed our previous work in low molecular weight metabolites, which demonstrated field effects near esophageal cancers(24). For cohort 2, lower esophageal mucosal biopsies were accrued from patients undergoing diagnostic/therapeutic endoscopy suite at St. Mary's Hospital. Tissue types were classified into healthy esophageal epithelium (HEE, i.e. from healthy volunteers rather than cancer-adjacent normal tissue), inflamed esophageal epithelium (IEE), Barrett's metaplasia (BM), Barrett's dysplasia (BD) or esophageal adenocarcinoma (EA) prior to any treatment. All samples were collected from within 5cm of the gastro-esophageal junction, apart from HEE, which was collected from between 15 and 5 cm. These groups were selected to assess the stepwise differences in GPL profiles along the carcinogenic sequence of EA, and also to externally validate the findings of Cohort 1. The histology of adjacent samples was independently verified by two histopathologists (R.G. and G.P.) with a specialist interest in upper gastro-intestinal cancer.

Exclusion criteria for both cohorts included patients with esophageal squamous cell carcinoma, malignancy associated with any other site in the body, other gastrointestinal tract pathology, liver disease and patients with signs/symptoms of acute infection. Demographic and clinical data including past medical history, drug history, chemotherapeutics, smoking status and alcohol intake history were recorded for all patients (see Supplementary Table 1 & 2). Histopathological variables including tumor type/differentiation/grade and stage, presence of perineural/lymphovascular invasion and lymph nodal metastases were recorded for patients in Cohort 1 (see Supplementary Table 1).

Desorption electrospray mass spectrometry imaging

Sample processing and acquisition of mass spectra

A schematic of the DESI-MSI workflow is given in Figure 1A. A fine stream of an ionised solvent (typically methanol and water) is "sprayed" onto a cryosectioned tissue specimen, which subsequently liberates ionised target species from the sample (often lipids). These are aspirated into a mass spectrometer, which generates a mass spectrum for this particular location on the section ("pixel"). An automatic stage controller then moves to the next pixel, and a mass spectrometry "image" is built up. Tissue destruction is minimal, so the post-DESI-MSI section can be histologically stained, co-registered with the mass spectrometry image, and used to supervise discriminative analysis. Complex multivariate statistics are then needed to process the large datasets that result from the highly resolved mass spectra, from a large number of pixels, across several sampling regions, across several patients, in order to build up a metabolomic profile.

All clinical tissue samples were snap frozen in liquid nitrogen immediately upon disconnection. Samples were stored at -80^{o}C for no longer than 1 month prior to cryo-

sectioning at 15μm and mounting on glass slides. All specimen processing was performed below -30^{o}C. Clinical sample analysis was performed in random order, constant instrument/environmental settings and in a brief time frame to avoid any batch effect influencing the results. DESI-MSI analysis was performed using an Exactive Fourier-Transform Orbitrap mass spectrometer (Thermo Fisher Scientific Inc., Bremen, Germany) controlled by XCalibur 2.1 software. Mass spectrometry data was acquired in negative ion mode in the *m/z* 150-1000 range. The spatial resolution for the imaging experiments was set to 75μm, corresponding to X/Y dimensions of the image pixels. Full protocol for optimisation, precision measurements and spectra acquisition are reported in a previous study(25).

Tissue sections were post-stained for histological confirmation and direct comparison was made with the mass spectrometry image (MSI) for cell/tissue specific data extraction. All samples were stained with H&E prior to digital imaging with a high-resolution digital microscope (NanoZoomer 2.0-HT digital slide scanner) and assessed by two blinded, consultant histopathologist for histological mapping of cell/tissue types within the specimens.

Tissue specific mass spectra extraction

Raw mass spectrometric data was converted to imzML format via imzML Converter (version 1.0.5)(26) and imported into MATLAB (R2014a) for feature extraction, pre-processing and data analysis using an in-house bio-informatics platform(27). Each MSI is composed of multiple pixels representing individual mass spectra. In order to extract relevant mass spectra of specific cell/tissue types the MSI must be compared to its matched histological image. As previously described, the histological image was assessed by an independent consultant histopathologist for identification and spatial mapping of specific cell/tissue types, which was recorded on digital imaging software (Nanozoomer, Hamamatsu).

The histological and MSI image were then aligned using an in-house–developed automated affine image transformation (translation, rotation, and scaling) algorithmic based on a gradient descent optimization approach(27). The co-registration of the matched histology and MSI permitted selection of mass spectra of specific tissue types by highlighting a corresponding two-dimensional area on the matched histology image. This process was repeated for each sample to extract mass spectra of each specific tissue type to populate a composite database. Within the database the mass spectra of each tissue type was also categorized with respect to its sample of origin in order to perform inter-sample comparisons.

Data Pre-processing

Negative ion mode data was acquired between the 150-1000 m/z range. Analysis of glycerophospholipids was performed on the 600-1000 m/z range. Analysis of fatty acids was performed on the 150-400 m/z range. Subsequent data pre-processing of the raw data was then performed on the selected m/z range of interest. Despite daily mass calibration of the Exactive Mass Spectrometer, non-linear mass shifts of common peaks were evident across multiple samples. To perform comparative analysis of multiple samples these mass shifts were corrected by means of an in-house peak alignment algorithm (dynamic programming, 8ppm matched)(28). To account for differential lipid density owing to differences in cell morphology, spectra were normalised to the Total Ion Count. Therefore, the only differences were in the ratios of the spectral features (corresponding to lipids in this case) found within that mass range. The spectra were then de-noised; peaks were identified as noise and eliminated if present in <50% of representative mass spectra of any tissue type. Finally, the mean average of selected pixels of each tissue type within each patient sample was calculated and stored as a single data unit.

Statistics

All analysis was conducted in Matlab, using a previously published toolbox (27). To illustrate the dataset in reduced dimensional space, principal components analysis was initially used as the unsupervised technique. As described, each tissue type from each sample was average across several sampling regions, such that each point indicated one tissue type from one sample. The supervised approach was recursive maximum margin criterion, and internally cross-validated models were generated using k-fold/leave one out cross validation. Misclassifications were visualised using confusion matrices. GPL/fatty acid annotations were made using LipidMAPS(30), after exclusion of isotopologues. The mean intensity values of lipids in different tissue subclasses (e.g. cancer versus proximal healthy epithelium) were compared by log2 transformed mean fold change. Lipid intensities between tissue subclasses were compared for statistically significant differences by ANOVA, with p-values adjusted to q values with a false discovery rate of 0.001, to reduce multiplicity error. Overall Class/Saturation/Acyl chain length comparisons of GPL between tissues were compared using ANOVA with Tukey post-hoc analysis. Further explanation of the statistical approach can be found in the Supplementary Methods.

Quantitative reverse transcriptase polymerase chain reaction

The MIQE guidelines were followed. Endoscopic biopsies (2-3 each) of EA and MHEE were collected as for DESI-MSI (replicate samples of Cohort 1). The samples were mounted in OCT, flank cryosectioned, and microdissected to achieve a target cellularity of >90%. The OCT was trimmed and the sample homogenised in Trizol (ThermoLIfe) using a three-step protocol involving (i) a hand-held oscillating pestle (ii) 30 seconds steel bead-beating (iii) passage of the homogenate through a Qiashredder (Qiagen). This optimised protocol was necessary to acquire adequate yield (>50ng) from small squamous samples while

maintaining RNA integrity (RIN > 7). RNA was then fractionated in according the Trizol instructions, and then additionally purified using RNEasy columns, with an extra wash step with both RW1 and RPE buffers. cDNA was made using SuperScript III (ThermoLIfe) and quantified using PowerSybr master mix and AB7900 thermal cycler all used according to the manufacturers' instructions. Controls without template did not amplify. GAPDH was selected as the internal control gene as this was the most stable across an initial run of 10 samples. Oligonucleotide details are provided in the Supplementary Methods.

Cell culture and transfection

The FLO1 EAC cell line was purchased from ECACC (Public Health England) at the start of the study, who had authenticated the line using short tandem repeat profiling. Cultures were mycoplasma tested every month (last tested 10th January 2020), and all experiments were conducted within 10 passages of the original stock. Cultures were established in conditions recommended by the accompanying literature. For RNA silencing experiments, cells were seeded onto glass cover-slips and transiently transfected with an ACLY-targeting siRNA, or non-targeting siRNA ("ControlScramble", Silencer Select, Ambion, control RNA 1), or water ("ControlVector"), using oligofectamine (Life) according to the manufacturer's instructions. After 48 hours, cells were washed twice in 150mM ammonium acetate, and snap frozen on the cover slip prior to direct DESI-MSI. Silencing efficiency was checked using immunoblotting of replicate wells as previously described (31), using the *ACLY* primary antibody 4223 (Cell Signalling Technologies). Selection of siRNA was based on sequence alignment to minimize off-target effects.

Immunohistochemistry

The expression of the key enzymes involved in the de novo lipogenesis pathway (ACLY, ACACA, FASN, SCD and ELOVL1) were assessed in EA and MHEE in twenty patients from Cohort 1. Fresh tissue samples adjacent to those taken for DESI-MSI and qPCR were fixed in formalin and mounted in wax. After sectioning, specimens were dewaxed, hydrated, and retrieved in Bond Epitope Retrieval Solution 1 for 20 minutes or Solution 2 for 40 minutes at 100 ^{o}C. Peroxidases were blocked, and the specimens were incubated with optimised concentrations of antibodies for 30-120 minutes (primary antibody details are in the Supplementary Methods). Primary antibody binding was visualised using Bond Polymer Refine Detection (DS9800, Leica). All staining procedures were carried out on a Leica Bond Autostainer.

Immunoreactivity scoring was independently undertaken by two histopathologists (R.G. and G.P.). The analysis was confined to cancer cells in the tumour samples versus squamous cells in the normal esophageal mucosa. The H-score method was used: score 0, 1, 2, 3 for intensity (negative, weak, moderate, and strong), multiplied by the percentage of staining cells, out of a maximum of 300. Median scores were calculated for the cancer and healthy mucosal groups for each lipogenic enzyme and compared by Mann-Witney U test with *a P* value <0.05 to define statistical significance.

Results

1. The GPL signature of esophageal adenocarcinoma

DESI-MSI was able to distinguish the tissue types within the complex EA microenvironment (see Figure 1B). A representative analysis is provided in Figure 1B-F, demonstrating differentiation between Barrett's metaplasia, Barrett's dysplasia and smooth muscle within a single section. Tissue architecture was preserved (Figure 1B). A multivariable model derived from across the GPL mass range (m/z 600 – 1000) segregated these groups in reduced dimensional space (Figure 1C,D). Specific discriminating lipids could be quantitatively visualised. For example, PI 34:1 was greatly enriched in Barrett's cells compared to adjacent smooth muscle, and most greatly in dysplastic Barrett's (m/z 835.5342, $P = 3.1 \times 10^{-32}$, see Figure 1E,F).

The glycerophospholipid signature of esophageal adenocarcinoma was characterised using two cohorts. Initially (Cohort 1), paired surgical resection biopsies (EA and matched healthy esophageal epithelium, MHEE) from 33 consecutive patients were profiled for GPL differences using DESI-MSI. This sampling approach was selected as the intended application was for operative margin analysis, and to overcome regional metabolomic differences in the tumour by sampling a larger specimen. Next a second cohort was sampled using endoscopic biopsies. This allowed specimens to be acquired from healthy volunteers and patients with Barrett's metaplasia/dysplasia. It also allowed us to validate findings from the first cohort, investigate the performance of the technique on small specimens, and demonstrate the second clinical application of facilitated diagnosis in the endoscopy suite.

Cohort 1: Discovery

The analytical pipeline calculated average mass spectra for each patient, by synthesising data within and between histologically verified sampling zones. Typically, for each specimen, 10-15 zones with ~100-200 pixels each were sampled (one pixel = one mass spectra), such that each phospholipidome represented at least 10,000 mass spectra. The demographics and case characteristics of this cohort of patients are included in Supplementary Table 1.

Unsupervised multivariate analysis of mass spectra in the *m/z* 600-1000 range demonstrated clear segregation between EA and MHEE (Figure 2A). Separation was apparent in the first component of the PCA, which explained 22.5% of the variance. This separation was more pronounced on supervised analysis (Figure 2B). After internal cross validation, the model correctly classified 93.9% of EA and MHEE (see Figure 2C and Supplementary Figure 1A), with two EA samples were incorrectly classified. The area-under-the-receiver-operated-characteristic curve (AUC) was 0.97 (see Supplementary Figure 1B).

A total of 192 GPLs were identified, with disparate abundances throughout the mass range (see Supplementary Figure 1C). In MHEE, phosphatidylethanolamines (PEs) and phosphatidylinositols (PIs) were the most abundant groups of GPLs, followed by phosphatidylserines (PSs), phosphatidylglycerols (PGs), and phosphatidic acids (PAs) (see Figure 2D). In EA there were significantly more PGs (ANOVA with Tukey, $P<0.0001$) and less PAs ($P<0.05$) and PEs ($P<0.001$), compared to MHEE (see Figure 2D).

The predominant GPL chain lengths had even numbers of carbon (34, 36, 38, and 40, i.e. various combinations of the C16:x, C18:x, and C20:x fatty acids, see Figure 2E). Compared to MHEE, there was a tendency towards longer acyl chain lengths with significantly more EA species with 37 ($P<0.05$), 39 ($P<0.01$), 40 ($P<0.0001$), 42 ($P<0.01$), 43 ($P<0.0001$) total acyl

carbons, and significantly less 33 (P<0.001) and 34 (P<0.0001) total acyl carbons (see Figure 2E). Significant differences also existed in odd chain GPLs despite very low abundances. Across the tissue types, GPL most frequently had 1, 2, or 4 desaturations (see Figure 2F). There was significantly less saturated and monounsaturated acyls in EA compared to MHEE (P<0.01), and significantly more polyunsaturated acyls (P<0.01, see Figure 2F). The GPL species which most significantly contributed to PE/PG, total acyl length and total acyl desaturation class differences are provided in Figure 2G-I respectively.

Specific differences in GPL species are provided in Supplementary Table 3, together with significantly different plasmalogens (i.e. monoacylglycerols) that were identified. Of the 20 most significantly enriched GPL species (ANOVA with FDR), 10 were PGs, and 9 were enriched in EA by at least 2 log2(fold change). Additional validation of GPL annotation by MS^2 (using the Exactive Orbitrap FTMS) was also possible for abundant molecular ions and is also provided in Supplementary Table 3. Examples of molecular and product ion scans are provided in Supplementary Figure 2A-H.

Cohort 2: Validation and stepwise differences

To validate these findings and understand if stepwise GPL differences occur with different stages of carcinogenesis (see Figure 3A), endoscopic biopsies from relevant patients were profiled using DESI-MSI with histopathological confirmation (HEE=33; IEE=8; BM=26; BD=7; EA=10). Supplementary Table 2 demonstrates the case characteristics of these patients; demographics were generally matched, except that the IEE cases were younger and acid-suppression medication was higher in the BM group.

To validate the findings from Cohort 1, the phospholipidomes of HEE and EA only were initially compared (see Supplementary Figure 3). Unsupervised multivariate analysis of mass

spectra in the *m/z* 600-1000 range demonstrated separation of the data points along the first principal component (Supplementary Figure 3A), with clear differences throughout the mass range (Supplementary Figure 3B). The derived cross-validated RMMC model from these data correctly identified 100% of both tissue types (Supplementary Figure 3C), providing an AUROC of 1 (Supplementary Figure 3D). The leading difference was an abundance of PGs, with longer acyl chain and more desaturations. These data verify mass spectrometry imaging-based phospholipidomics as an accurate means of esophageal tissue recognition.

To assess for stepwise differences through transformation, phospholipidomes of the remaining tissue types were added to the analysis. Unsupervised multivariate analysis of mass spectra in the *m/z* 600-1000 range also demonstrated separation of data points along the first principal component between HEE/IEE to BM/BD/EA (Figure 3B), suggesting the leading GPL profiles differences are due to the squamous or columnar phenotypes. Supervised analysis using recursive maximum margin criterion verified segregation based on tissue-of-origin (Figure 3C). However, there was further clustering of EA from BM/BD along the second component, associating further GPL reprogramming with transformation. Internal cross-validation incorrectly classified one squamous sample as columnar; however, BD was more frequently misclassified as either BM or EA (Figure 3D).

The relative abundance of the 196 identified GPLs (*m/z* 600-1000 range) were compared, in terms of GPL class, acyl chain length and desaturations (Figure 3E-G). The relative quantity of PGs was higher in EA/BD/BM compared to HEE/IEE ($P<0.01$). The relative quantity of PIs was higher in BM/BD compared to HEE ($P<0.05$). The relatively quantity of PSs was lower in BM/BD/EA compared to HEE ($P<0.0001$) and IEE ($P<0.05$).

Overall, acyl chain length was longer in BM/BD/EA, with significantly greater concentrations of 37, 38, and 40 carbon lengths, and less chains of 34 (Figure 3F). Acyl chains from BM/BD/EA had more desaturations, including significantly more having 4 or more double-

bonds, and significantly less having less than 2 (Figure 3G). In summary, GPLs of BM/BD/EA were enriched for PGs, and had longer acyl chains with more desaturations.

To understand whether the GPL signature changes during progression to invasive cancer, we compared univariate PG characteristics between EA with BM, as this class was most enriched in cancer (Figure 3E and Supplementary Table 4). Comparison of individual GPLs showed a significant increase in six long-chain polyunsaturated PGs ($q<0.001$), with PG (42:8) having the greatest increase (log2 fold change 6.1, ANOVA $q = 8.6 \times 10^{-4}$). The other enriched PGs were PG (38:4), (38:5), (38:6), (40:5), and (40:6).

2. Drivers of the EA glycerophospholipid signature

The EA fatty acid profile

Long chain fatty acids (FAs) of 12-26 carbon atoms are used to make GPL acyl chains in humans(8), so profiling the fatty acid pool may offer mechanistic insights into GPL acyl characteristics. The relative abundance of FAs found within the *m/z* 150-400 range were compared between EA and MHEE from Cohort 1. In unsupervised analysis using data from this mass range only, there was separation of the datapoints along the third component, which explained 8.9% of the variance (Figure 4A). This separation was more pronounced in supervised analysis (Figure 4B). Internal cross validation correctly classified 87.9% of EA and 90.9% of MHEE based on the FA profiles of the samples, with an AUC of 0.96 (Figure 4C). FA acyls had significantly less 16-carbon chains in EA, and significantly more with longer chains (see Figure 4D,E). There were also significantly less saturated FA acyls in EA and significantly more desaturated acyls (see Figure 4F,G).

Genetic basis for GPL signature and contribution of *de novo* lipogenesis

We hypothesised that GPL class-switch was driven by corresponding changes in gene expression. To test this hypothesis and generate candidates, we checked whether the KEGG GPL gene set was significantly altered in an archived transcriptomic dataset for EA and HEE (GSE 26886). Overall, EA was significantly enriched for GPL synthetic genes (see Figure 5A). To explore this further, we extracted mRNA from endoscopic biopsies of HEE and EA (n = 20 each), and quantified the expression of the most significantly altered candidates (see Figure 5B,C). Genes involved in PG synthesis, both by diacylglycerol phosphorylation and by lyso-PG acylation, were strongly enriched in EA compared to HEE (median fold change 2.5 (LPGAT) and 8.3 (PGS1) both P <0.001). The final synthetic step in PG metabolism – dimerization by *CRLS1* to cardiolipin – was also upregulated in EA.

We then checked whether genes involved in fatty acid synthesis were also deregulated in EA, using immunohistochemistry. This revealed robust EA expression of *ACYL, FASN, EVOVL1, ACACA,* and *SCD* that was at least equivalent to or greater than MHEE (see Figure 5D and Supplementary Figure 4A). Given that both the FA and GPL-acyl pools of EA had similar characteristics, and that genes involved in *de novo* lipogenesis were active in EA, it was hypothesised that *de novo* lipogenesis contributes to GPL acyl reprogramming. To test this, *ACYL* was silenced in FLO1 EA cells *in vitro*, and the resulting GPL signature was measured with DESI-MSI (Supplementary Figure 4B,C). *ACYL* channels carbon from the citrate cycle to acetyl CoA, thus providing the materials for acyl elongation, and is considered the first committed step in carbon shuttling to lipid anabolism(32). After 72h, there were significantly less GPLs with total acyl chain length of 40, and significantly more with 36 carbons (see Figure 5E). In summary, genes involved in GPL and *de novo* fatty acid synthesis were broadly enriched in EA, and impairing *de novo* lipogenesis in EA cells reverted GPL acyls toward a normal phenotype.

Discussion

In this study, we combined DESI-MSI lipidomic profiling with gene expression and perturbation studies to describe the GPL signature of EA, and its genetic basis. In two consecutive tissue series, sampled surgically and then endoscopically, multivariable models based derived from glycerophospholipid profiles were highly discriminant for EA compared to squamous and other control tissue (AUROC = 0.97 and 1). These results suggest DESI-MSI can differentiate tissue-types in the malignant esophagus. Potential clinical applications include objective diagnosis and intra-operative margin assessment, especially given recent reports of rapid processing times(33).

There was stepwise enrichment of PGs from normal to malignant tissue samples. Small concentrations of PGs can have potent effects on signalling(14,34,35), and PGs are usually at trace concentrations in mammalian tissues. In EA, PGs were the third most abundant GPL class, and how this significant increase in PG affects EA signalling requires further study. PGs are also the precursors of cardiolipins, which contribute to mitochondrial functionality and are frequently altered in cancer states(36),(37,38). PIs were particularly enriched in BM/BD. Given the interest in PI3K signalling to EA(39), this observation also warrants further investigation. The decrease in PS concentration may also be pro-tumorigenic, as PS is a pro-apoptotic signalling molecule and a chemoattractant for macrophages and other immune cells(40). The significance of the slight decrease in PAs is less clear and may reflect increased lipase activity leading to PG and PI-enrichment.

Acyl chains of EA GPLs had more desaturations and longer lengths, which probably reflect corresponding changes in the fatty acid pool. Genes which *de novo* synthesise, extend and desaturate fatty acids were strongly expressed in EA. In ovarian cancer, desaturases support cancer stemness and drive nf-κB signalling(41). Elongase activity and longer acyl chain lengths have been associated with a pro-cancer phenotype in lung(42,43),

prostate(44) and breast cancers(45), implying that these characteristics confer ligand activity. Recently it was demonstrated that different PG species have contrasting effects on mouse skin keratinocyte proliferation(14). Similar species-specific effect has been demonstrated for cardiolipins(38). In the present dataset some EA lipids were up to 70x enriched, and an important next step with be the functional annotation of these discriminatory lipids within EA signalling.

A strength of this paper was to begin to describe the underlying genetic and mechanistic basis of phospholipid reprogramming. Genes that control *de novo* lipogenesis and GPL synthesis were generally upregulated in EA, implying diversion to the final products of GPL metabolism (e.g. PIs, cardiolipins). Our finding that *ACLY* silencing reduces GPL chain length supports the hypothesis that these phenotypes are partly explained by acetyl CoA-derived *de novo* lipogenesis and/or elongation (32), which is also supported by the observed robust expression of relevant lipogenic genes. Recently, mTORC2 was shown to be a master regulator of GPL synthesis, and is hyperactive in EA(46); however, the complete coordination of de novo lipogenesis is likely multifactorial. Additionally, the promoter of *PTDSS1* is frequently mutated in EA(13), which suggests lipid reprogramming is selected in oncogenesis. It should be stressed that the *ACLY* experiment constitutes a technical and biological proof-of-principle, and a more comprehensive functional and mechanistic assessment of the effects of deregulated lipogenic genes is needed.

Additional strengths include the use of complementary independent cohorts of patient samples to corroborate our lipidomic findings; transparent details of patient selection; the use of multiple control samples that where either matched to the tumour from the resection specimen (cohort 1) or matched in terms of demographics, medication and lifestyle factors (cohort 2); gold standard determination by two expert histopathologists and a robust methodology for data analysis and interpretation. This study's limitations include the sample sizes of BM/BD and the single analytical platform for lipidomic profiling. Additionally, the

present study did not assess the signatures of minor lipid classes such as cholesterols, ceramides and sphingomyelins. Future studies should use externally calibrated MS/MS validation, supported by molecular studies to test the relevance of the lipid species and genes on the overall phenotype. Specific inhibitors are available for lipogenic genes(47,48), and thus these findings may indicate new therapeutic avenues.

In conclusion, DESI-MSI can objectively recognise adenocarcinoma in the esophagus. The EA phospholipidome is greatly enriched for long-chain, polyunsaturated PGs, and genetic studies suggest an orchestrated mechanism linked to *de novo* lipogenesis. The functional effect of the discriminatory lipids remains to be determined.

References

1. Torre LA, Bray F, Siegel RL, Ferlay J, Lortet-Tieulent J, Jemal A. Global cancer statistics, 2012. CA Cancer J Clin. 2015;65:87–108.
2. Enzinger PC, Mayer RJ. Esophageal cancer. N Engl J Med. 2003;349:2241–52.
3. Chadwick G, Varagunam M, Maynard N, Brand C, Cromwell D, Riley S, et al. National Oesophago-Gastric Cancer Audit 2016 [Internet]. R. Coll. Surg. Engl. 2016.
4. Hanahan D, Weinberg RA. The hallmarks of cancer. Cell. 2000;100:57–70.
5. Kroemer G, Pouyssegur J. Tumor Cell Metabolism: Cancer's Achilles' Heel. Cancer Cell. 2008;13:472–82.
6. Holmes E, Wilson ID, Nicholson JK. Metabolic Phenotyping in Health and Disease. Cell. 2008;134:714–7.
7. Wishart DS, Knox C, Guo AC, Eisner R, Young N, Gautam B, et al. HMDB: a knowledgebase for the human metabolome. Nucleic Acids Res. 2009;37:D603–10.
8. Wenk MR. The emerging field of lipidomics. Nat Rev Drug Discov. 2005;4:594–610.
9. Rahman SMJ, Gonzalez AL, Li M, Seeley EH, Zimmerman LJ, Zhang XJ, et al. Lung Cancer Diagnosis from Proteomic Analysis of Preinvasive Lesions. Cancer Res. 2011;71:3009–17.
10. Eberlin LS, Norton I, Dill AL, Golby AJ, Ligon KL, Santagata S, et al. Classifying Human Brain Tumors by Lipid Imaging with Mass Spectrometry. Cancer Res. 2011;72:645–54.
11. Guenther S, Muirhead LJ, Speller AVM, Golf O, Strittmatter N, Ramakrishnan R, et al. Spatially Resolved Metabolic Phenotyping of Breast Cancer by Desorption Electrospray Ionization Mass Spectrometry. Cancer Res. 2015;75:1828–37.
12. Dória ML, McKenzie JS, Mroz A, Phelps DL, Speller A, Rosini F, et al. Epithelial ovarian carcinoma diagnosis by desorption electrospray ionization mass spectrometry imaging. Sci Rep. 2016;6:39219.

13. Frankell AM, Jammula S, Li X, Contino G, Killcoyne S, Abbas S, et al. The landscape of selection in 551 esophageal adenocarcinomas defines genomic biomarkers for the clinic. Nat Genet. 2019;51:506–16.
14. Xie D, Seremwe M, Edwards JG, Podolsky R, Bollag WB. Distinct effects of different phosphatidylglycerol species on mouse keratinocyte proliferation. PLoS One. 2014;9:e107119.
15. Sommer U, Herscovitz H, Welty FK, Costello CE. LC-MS-based method for the qualitative and quantitative analysis of complex lipid mixtures. J Lipid Res. 2006;47:804–14.
16. Pulfer M, Murphy RC. Electrospray mass spectrometry of phospholipids. Mass Spectrom Rev. 2003;22:332–64.
17. McDonnell LA, Heeren RMA. Imaging mass spectrometry. Mass Spectrom Rev. 2007;26:606–43.
18. Gode D, Volmer DA. Lipid imaging by mass spectrometry – a review. Analyst. 2013;138:1289.
19. Jarmusch AK, Pirro V, Baird Z, Hattab EM, Cohen-Gadol AA, Cooks RG. Lipid and metabolite profiles of human brain tumors by desorption electrospray ionization-MS. Proc Natl Acad Sci U S A. 2016;113:1486–91.
20. Banerjee S, Zare RN, Tibshirani RJ, Kunder CA, Nolley R, Fan R, et al. Diagnosis of prostate cancer by desorption electrospray ionization mass spectrometric imaging of small metabolites and lipids. Proc Natl Acad Sci U S A. 2017;114:3334–9.
21. Gouw AM, Eberlin LS, Margulis K, Sullivan DK, Toal GG, Tong L, et al. Oncogene KRAS activates fatty acid synthase, resulting in specific ERK and lipid signatures associated with lung adenocarcinoma. Proc Natl Acad Sci U S A. 2017;114:4300–5.
22. Abbassi-Ghadi N, Golf O, Kumar S, Antonowicz S, McKenzie JS, Huang J, et al. Imaging of Esophageal Lymph Node Metastases by Desorption Electrospray Ionization Mass Spectrometry. Cancer Res. 2016;76:5647–56.
23. McShane LM, Altman DG, Sauerbrei W, Taube SE, Gion M, Clark GM. Reporting

Recommendations for Tumor Marker Prognostic Studies (REMARK). JNCI J Natl Cancer Inst. 2005;97:1180–4.

24. Yakoub D, Keun HC, Goldin R, Hanna GB. Metabolic profiling detects field effects in nondysplastic tissue from esophageal cancer patients. Cancer Res. 2010;70:9129–36.

25. Abbassi-Ghadi N, Jones EA, Veselkov KA, Huang J, Kumar S, Strittmatter N, et al. Repeatability and reproducibility of desorption electrospray ionization-mass spectrometry (DESI-MS) for the imaging analysis of human cancer tissue: a gateway for clinical applications. Anal Methods. 2015;7:71–80.

26. Schramm T, Hester Z, Klinkert I, Both J-P, Heeren RMA, Brunelle A, et al. imzML — A common data format for the flexible exchange and processing of mass spectrometry imaging data. J Proteomics. 2012;75:5106–10.

27. Veselkov KA, Mirnezami R, Strittmatter N, Goldin RD, Kinross J, Speller AVM, et al. Chemo-informatic strategy for imaging mass spectrometry-based hyperspectral profiling of lipid signatures in colorectal cancer. Proc Natl Acad Sci. 2014;111:1216–21.

28. Inglese P, McKenzie JS, Mroz A, Kinross J, Veselkov K, Holmes E, et al. Deep learning and 3D-DESI imaging reveal the hidden metabolic heterogeneity of cancer. Chem Sci. 2017;8:3500–11.

29. Zhang H, Yang S, Guo L, Zhao Y, Shao F, Chen F. Comparisons of isomiR patterns and classification performance using the rank-based MANOVA and 10-fold cross-validation. Gene. 2015;569:21–6.

30. Schmelzer K, Fahy E, Subramaniam S, Dennis EA. The Lipid Maps Initiative in Lipidomics. Methods Enzymol. 2007 [2019 Jun 26]. page 171–83.

31. Tan SLW, Chadha S, Liu Y, Gabasova E, Perera D, Ahmed K, et al. A Class of Environmental and Endogenous Toxins Induces BRCA2 Haploinsufficiency and Genome Instability. Cell. 2017;169:1105-1118.e15.

32. Hatzivassiliou G, Zhao F, Bauer DE, Andreadis C, Shaw AN, Dhanak D, et al. ATP

citrate lyase inhibition can suppress tumor cell growth. Cancer Cell. 2005;8:311–21.

33. Pirro V, Alfaro CM, Jarmusch AK, Hattab EM, Cohen-Gadol AA, Cooks RG. Intraoperative assessment of tumor margins during glioma resection by desorption electrospray ionization-mass spectrometry. Proc Natl Acad Sci U S A. 2017;114:6700–5.

34. Kandasamy P, Numata M, Berry KZ, Fickes R, Leslie CC, Murphy RC, et al. Structural analogs of pulmonary surfactant phosphatidylglycerol inhibit toll-like receptor 2 and 4 signaling. J Lipid Res. 2016;57:993–1005.

35. Furse S. Is phosphatidylglycerol essential for terrestrial life? J. Chem. Biol. 2017.

36. Wallace DC. Mitochondria and cancer. Nat Rev Cancer. 2012;12:685–98.

37. Kiebish MA, Han X, Cheng H, Chuang JH, Seyfried TN. Cardiolipin and electron transport chain abnormalities in mouse brain tumor mitochondria: lipidomic evidence supporting the Warburg theory of cancer. J Lipid Res. 2008;49:2545–56.

38. Schild L, Lendeckel U, Gardemann A, Wiswedel I, Schmidt CA, Wolke C, et al. Composition of molecular cardiolipin species correlates with proliferation of lymphocytes. Exp Biol Med. 2012;237:372–9.

39. Kim J, Bowlby R, Mungall AJ, Robertson AG, Odze RD, Cherniack AD, et al. Integrated genomic characterization of oesophageal carcinoma. Nature. 2017;541:169–75.

40. Segawa K, Nagata S. An Apoptotic ‘Eat Me’ Signal: Phosphatidylserine Exposure. Trends Cell Biol. 2015;25:639–50.

41. Li J, Condello S, Thomes-Pepin J, Ma X, Xia Y, Hurley TD, et al. Lipid Desaturation Is a Metabolic Marker and Therapeutic Target of Ovarian Cancer Stem Cells. Cell Stem Cell. 2017;20:303-314.e5.

42. Marien E, Meister M, Muley T, Gomez Del Pulgar T, Derua R, Spraggins JM, et al. Phospholipid profiling identifies acyl chain elongation as a ubiquitous trait and potential target for the treatment of lung squamous cell carcinoma. Oncotarget. 2016;7:12582–97.

43. Marien E, Meister M, Muley T, Fieuws S, Bordel S, Derua R, et al. Non-small cell lung cancer is characterized by dramatic changes in phospholipid profiles. Int J Cancer. 2015;137:1539.
44. Tamura K, Makino A, Hullin-Matsuda F, Kobayashi T, Furihata M, Chung S, et al. Novel Lipogenic Enzyme ELOVL7 Is Involved in Prostate Cancer Growth through Saturated Long-Chain Fatty Acid Metabolism. Cancer Res. 2009;69:8133–40.
45. Yamashita Y, Nishiumi S, Kono S, Takao S, Azuma T, Yoshida M. Differences in elongation of very long chain fatty acids and fatty acid metabolism between triple-negative and hormone receptor-positive breast cancer. BMC Cancer. 2017;17:589.
46. Guri Y, Colombi M, Dazert E, Riezman I, Riezman H, Hall MN. mTORC2 Promotes Tumorigenesis via Lipid Synthesis. Cancer Cell. 2017;32:807-823.e12.
47. Peck B, Schulze A. Lipid desaturation - the next step in targeting lipogenesis in cancer? FEBS J. 2016;283:2767–78.
48. Flavin R, Peluso S, Nguyen P, Loda M. Fatty acid synthase as a potential therapeutic target in cancer. Futur Oncol. 2010;6:551–62.

Figure Legends

Figure 1: DESI-MSI workflow and representative section.

A. Schematic of the DESI-MSI workflow B. Post-DESI-MSI haematoxylin and eosin stain of a representative esophageal biopsy section. Zoning for different tissue types demonstrated; esophageal smooth muscle (Muscle, pink); Barrett's metaplasia (BM, green); Barrett's dysplasia (BD, red). 100 **μ**m C. Aligned false colour image of spatially-resolved total ion chromatogram D. Corresponding principal component analysis for (C) E. False colour image of PI 34:1 concentration across the tissue specimen (extracted ion chromatogram, m/z 835.3542) F. Concentrations of PI 34:1 in the tissue types.

Figure 2: Glycerophospholipid signatures of esophageal adenocarcinoma and matched healthy esophageal epithelium (Cohort 1).

A. Principal components analysis (PCA) of averaged mass spectra (*m/z* 600-1000) of esophageal adenocarcinoma (EA, red) versus matched healthy esophageal epithelium (MHEE, green) of patients in Cohort 1 (each dot = averaged spectra from one tissue type from one patient; each patient provided both EA and MHEE samples). B. Recursive Maximum Margin criterion (RMMC) supervised analysis score plot C. Leave one out cross-validated RMMC score plot. D-F Relative abundance of glycerophospholipids (GPL), by (D) class, (E) acyl chain length, and (F) desaturations. G-I GPL species that were significantly different ($q < 0.001$), by (G) class, (H) acyl chain length, and (I) desaturations. Groups were compared by ANOVA (with Tukey's HSD): $^{*}P<0.05$; $^{**}P<0.01$; $^{***}P< 0.001$. PS, phosphatidylserines; PI, phosphatidylinositol; PG, phosphatidylglycerol; PE, phosphatidylethanolamine; PA, phosphatidic acid.

Figure 3: Glycerophospholipid signatures of esophageal and various control tissues (Cohort 2).

A. Representative histology of healthy esophageal epithelium, inflamed esophageal epithelium, Barrett's metaplasia, Barrett's dysplasia and esophageal adenocarcinoma. Colour coding for rest of figure provided B. Principal components analysis of averaged mass spectra (*m/z* 600-1000) of the five tissue-types of patients in Cohort 2 (each dot = averaged spectra from one tissue type from one patient; each patient provided one tissue type only). C. Recursive Maximum Margin criterion (RMMC) supervised analysis score plot D. Leave one out cross-validated RMMC score plot as per confusion matrix; E-G. Relative abundances of GPLs (*m/z* 600-1000 range) grouped in terms of (E) class (F) acyl chain length and (G) desaturations. Groups were compared by ANOVA (with Tukey's HSD): **P*<0.05; ***P*<0.01; ****P*< 0.001. PS, phosphatidylserines; PI, phosphatidylinositol; PG, phosphatidylglycerol; PE, phosphatidylethanolamine; PA, phosphatidic acid.

Figure 4: Fatty acids signatures of esophageal adenocarcinoma and matched healthy esophageal epithelium in Cohort 1.

A. Principal components analysis (PCA) of averaged mass spectra (*m/z* 150-400) of esophageal adenocarcinoma (EA, red) versus matched healthy esophageal epithelium (MHEE, green) of patients in Cohort 1 (each dot = averaged spectra from one tissue type from one patient; each patient provided both EA and MHEE samples). B. Recursive Maximum Margin criterion (RMMC) supervised analysis score plot C. Leave one out cross-validated RMMC score plot. D-G Relative abundance of FAs (*m/z* 150-400), grouped by (D) acyl chain length, and (F) desaturations. E,G FA species that were significantly different (q <0.001), by (E) acyl chain length, and (G) desaturations. Groups were compared by ANOVA (with Tukey's HSD): **P*<0.05; ***P*<0.01; ****P*< 0.001.

Figure 5: The genetic framework of esophageal adenocarcinoma glycerophospholipid metabolism

A. Geneset enrichment score plot of the GPL metabolism geneset in GSE 26886. B. Overview of GPL metabolism with schematics of the various GPL classes. C. Relative GPL gene expression between esophageal adenocarcinoma (cancer, EA) and matched healthy esophageal epithelium (normal, MHEE). D. Representative immunohistochemistry sections of the five FA metabolism genes in EA and MHEE. Bar applies to all images and represents 100 **μ**m E. Relative abundance of acyl chain lengths in FLO1 EA cells transfected with siRNA targeting *ACLY* and relevant controls. *P* values calculated with Mann-Whitney U test for qPCR experiments, and ANOVA with Tukey HSD for GPL profiling experiments **P*<0.05; ***P*<0.01; ****P*< 0.001; *****P*< 0.001. PS, phosphatidylserines; PI, phosphatidylinositol; PG, phosphatidylglycerol; PE, phosphatidylethanolamine; PA, phosphatidic acid, PC, phosphatidylcholine; DAG, diacylglycerol; DAG-3P, diacylglycerol-triphosphate; CDP-DAG cytidine diphosphate diacylglycerol.

Figure 1

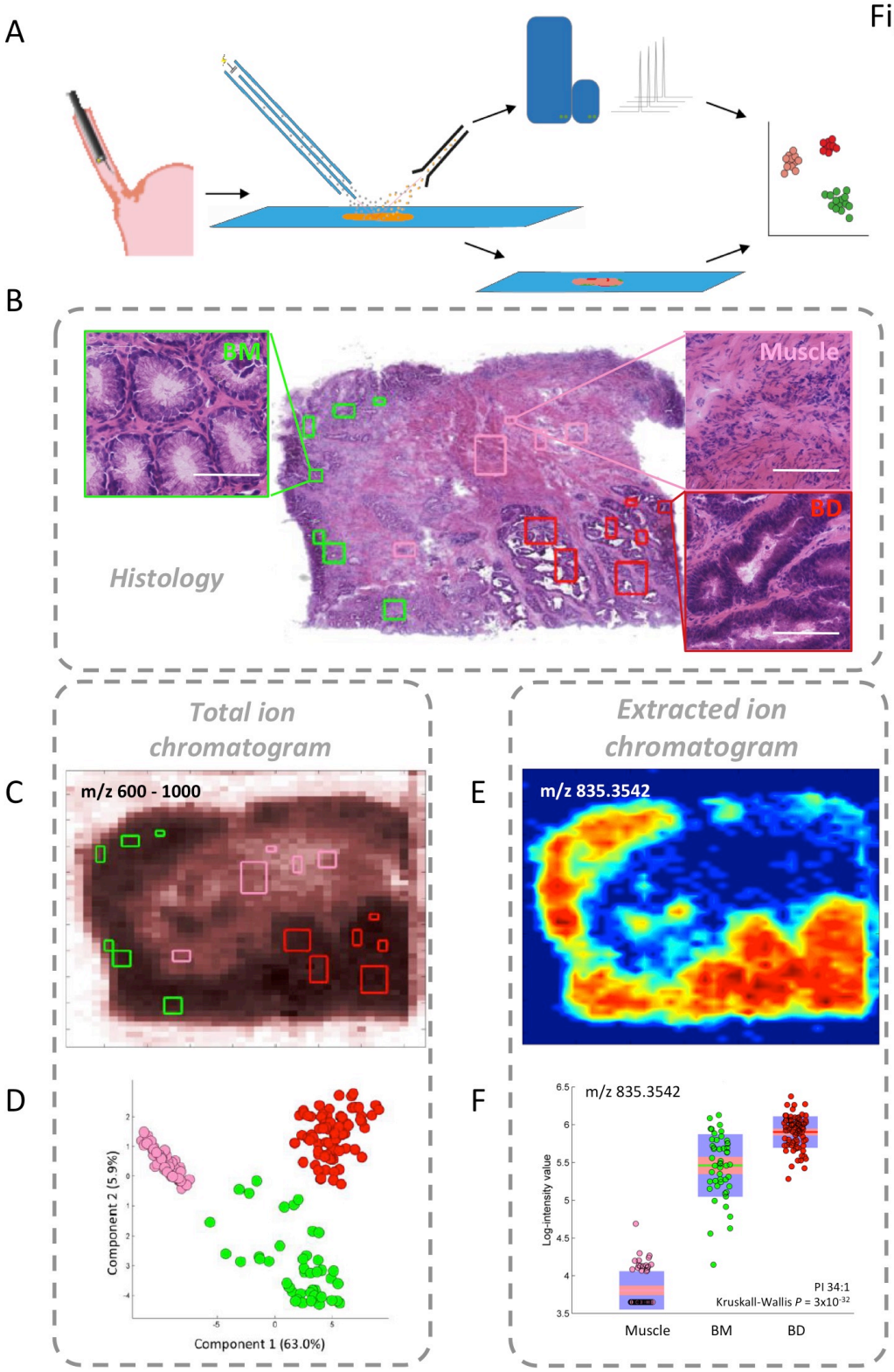
A
B
BM
Muscle
BD
Histology
Total ion chromatogram
Extracted ion chromatogram
C
m/z 600 - 1000
E
m/z 835.3542
D
Component 2 (5.9%)
Component 1 (63.0%)
F
m/z 835.3542
Log-intensity value
PI 34:1
Kruskall-Wallis P = 3x10-32
Muscle
BM
BD

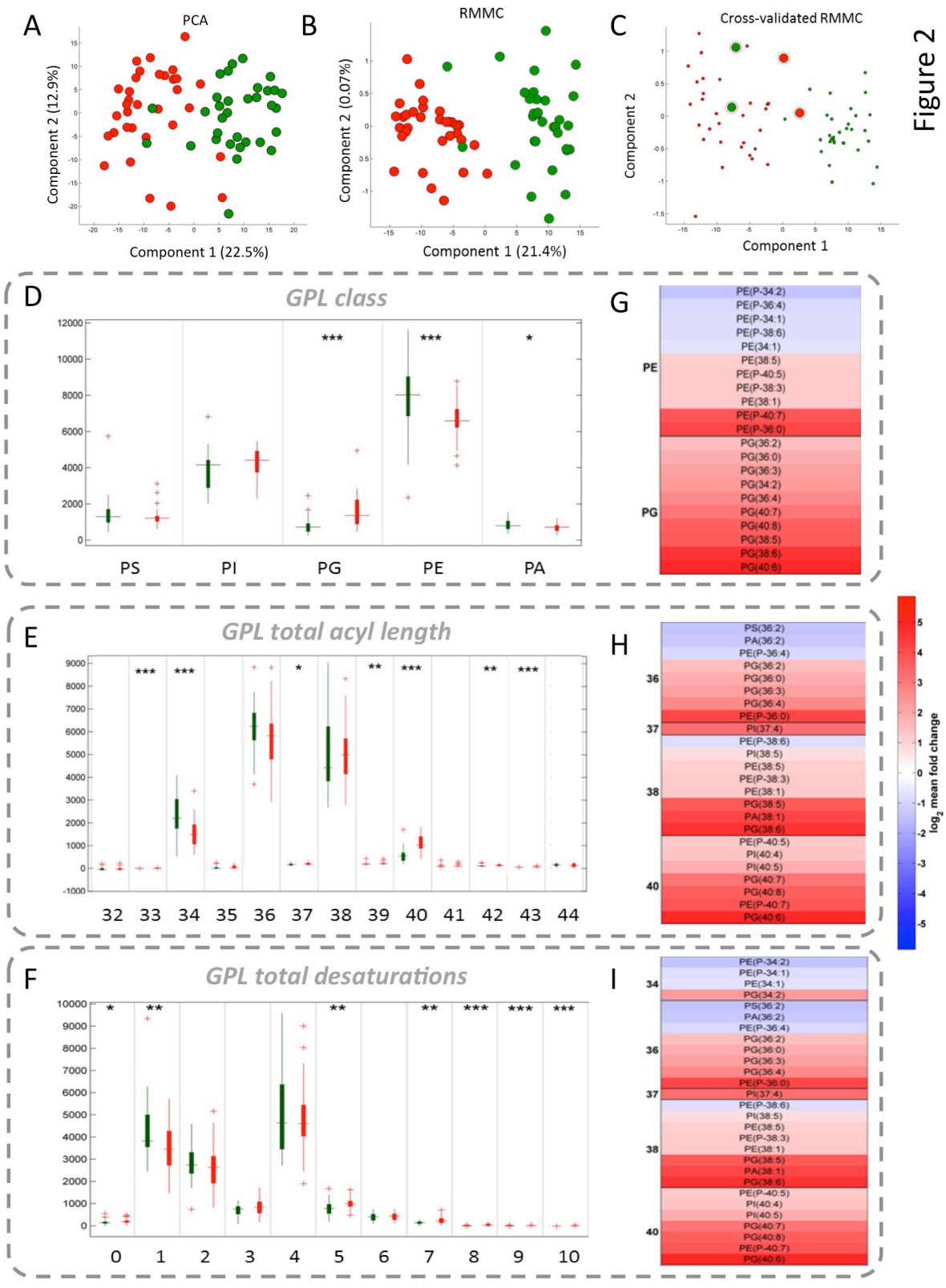
A
PCA
Component 2 (12.9%)
Component 1 (22.5%)
B
RMMC
Component 2 (0.07%)
Component 1 (21.4%)
C
Cross-validated RMMC
Component 2
Component 1
D
GPL class
PS
PI
PG
PE
PA
G
PE
PG
E
GPL total acyl length
H
I
F
GPL total desaturations
log2 mean fold change

Figure 2

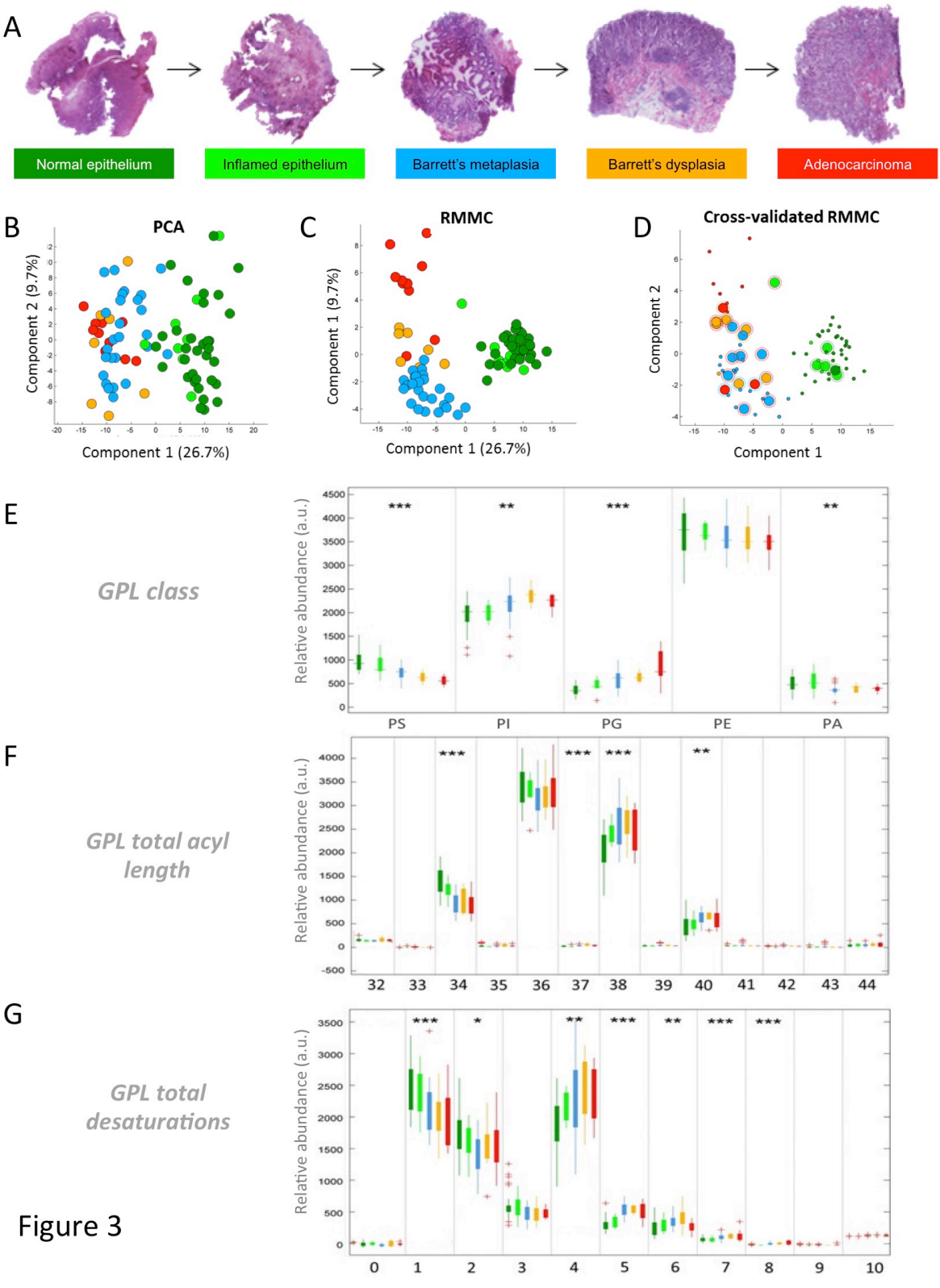
A
Normal epithelium
Inflamed epithelium
Barrett's metaplasia
Barrett's dysplasia
Adenocarcinoma
B
PCA
Component 2 (9.7%)
Component 1 (26.7%)
C
RMMC
Component 1 (9.7%)
Component 1 (26.7%)
D
Cross-validated RMMC
Component 2
Component 1
E
GPL class
Relative abundance (a.u.)
PS
PI
PG
PE
PA
F
GPL total acyl length
Relative abundance (a.u.)
G
GPL total desaturations
Relative abundance (a.u.)

Figure 3

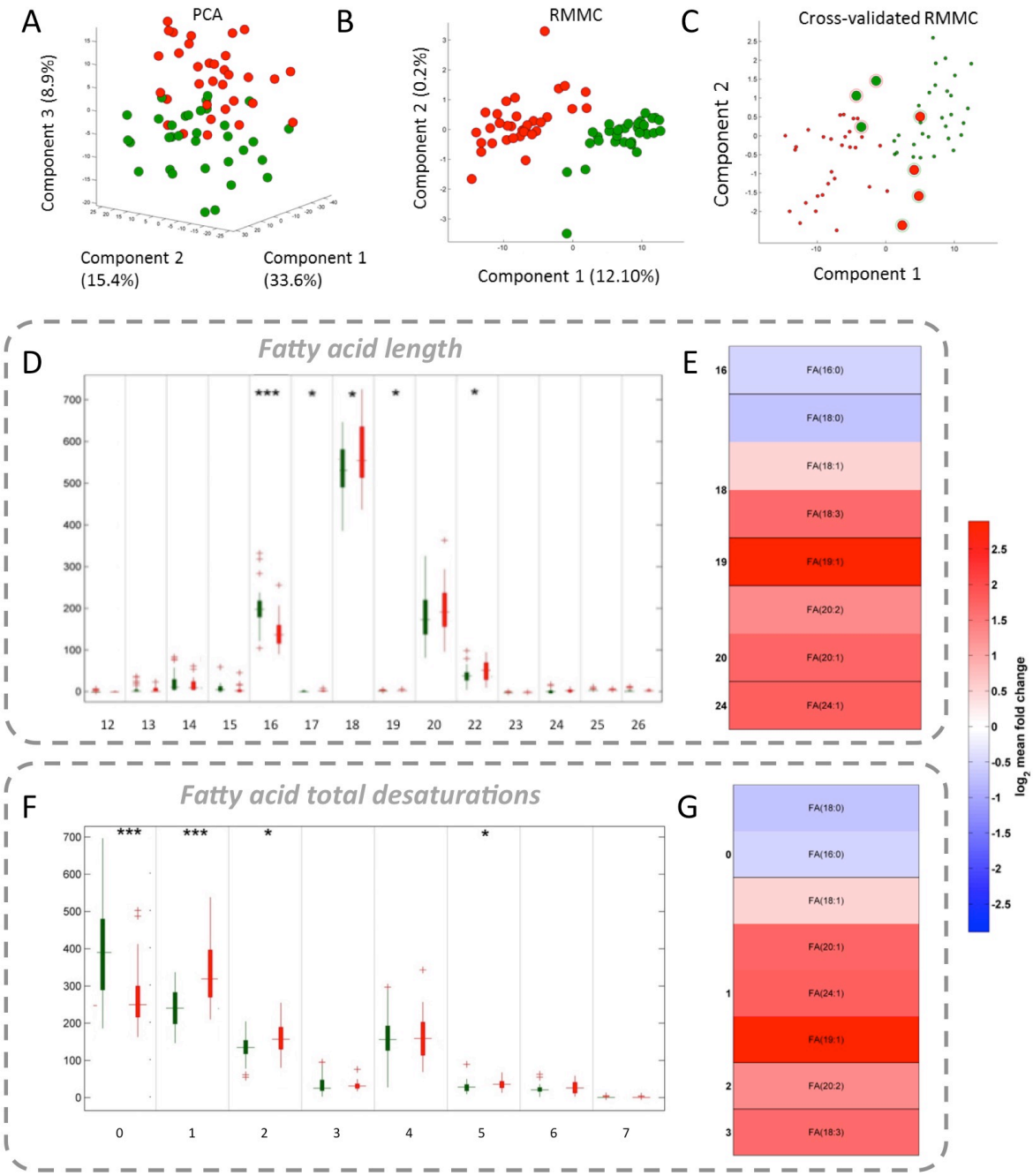
A
PCA
Component 3 (8.9%)
Component 2 (15.4%)
Component 1 (33.6%)
B
RMMC
Component 2 (0.2%)
Component 1 (12.10%)
C
Cross-validated RMMC
Component 2
Component 1
D
Fatty acid length
E
FA(16:0)
FA(18:0)
FA(18:1)
FA(18:3)
FA(19:1)
FA(20:2)
FA(20:1)
FA(24:1)
log2 mean fold change
F
Fatty acid total desaturations
G
FA(18:0)
FA(16:0)
FA(18:1)
FA(20:1)
FA(24:1)
FA(19:1)
FA(20:2)
FA(18:3)

Figure 4

1
2

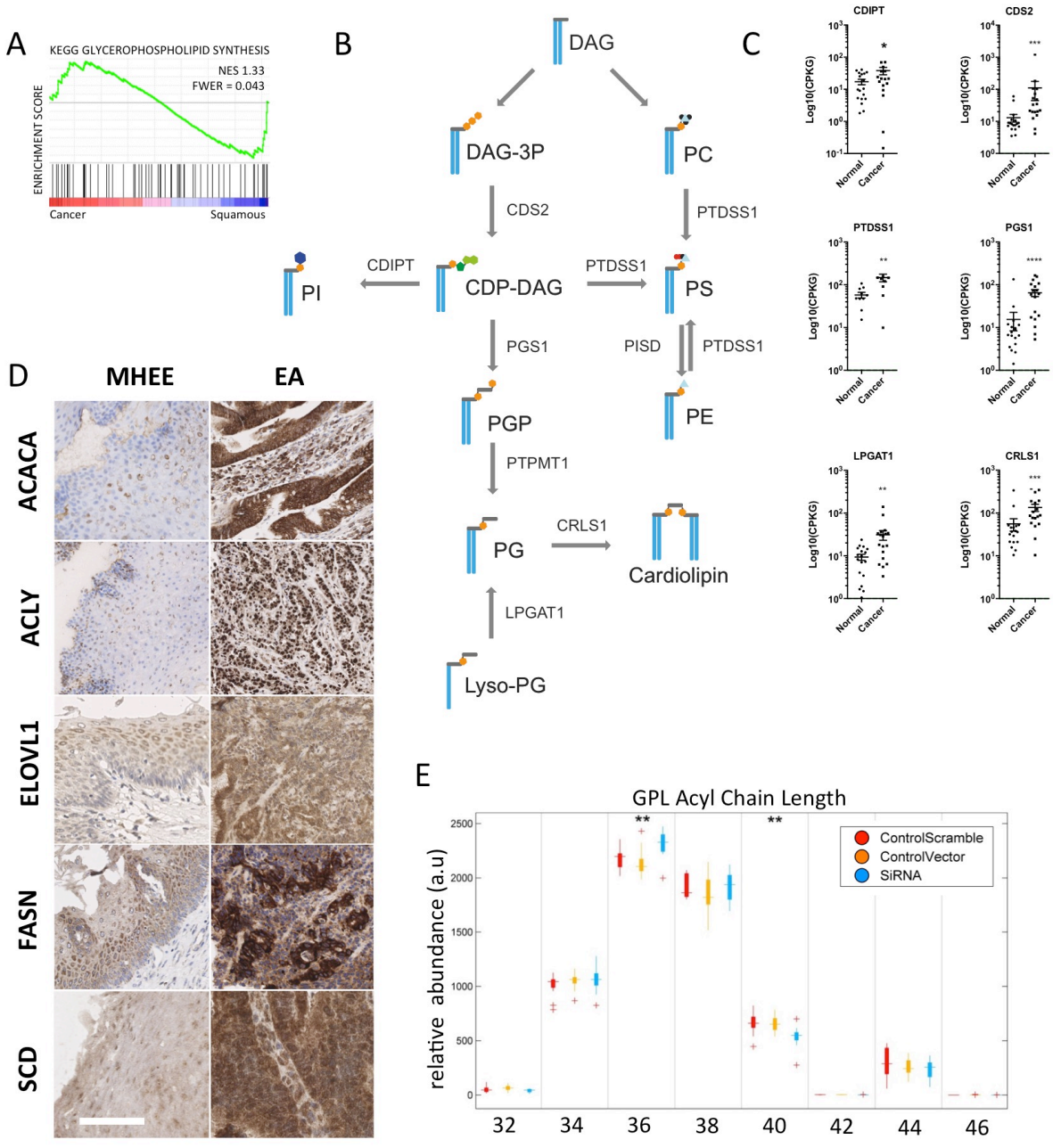
A
KEGG GLYCEROPHOSPHOLIPID SYNTHESIS
NES 1.33
FWER = 0.043
ENRICHMENT SCORE
Cancer
Squamous
B
DAG
DAG-3P
PC
CDS2
PTDSS1
PI
CDIPT
CDP-DAG
PTDSS1
PS
PGS1
PISD
PTDSS1
PGP
PE
PTPMT1
PG
CRLS1
Cardiolipin
LPGAT1
Lyso-PG
C
CDIPT
CDS2
PTDSS1
PGS1
LPGAT1
CRLS1
Log10(CPKG)
Normal
Cancer
D
MHEE
EA
ACACA
ACLY
ELOVL1
FASN
SCD
E
GPL Acyl Chain Length
relative abundance (a.u)
ControlScramble
ControlVector
SiRNA
32
34
36
38
40
42
44
46

Figure 5

1